PROCEEDINGS OF SCIENCE

ONLINE ICRC 2021 THE ASTROPARTICLE PHYSICS CONFERENCE Berlin | Germany 37th International Cosmic Ray Conference 12–23 July 2021

Modelling Phase-resolved Spectra and Energy-dependent Light Curves of the Vela Pulsar to Scrutinize its GeV Emission Mechanism

Monica Barnard,[a,b,*] **Christo Venter,**[a] **Alice K. Harding,**[c] **Constantinos Kalapotharakos**[d,e,f] **and Tyrel J. Johnson**[g]

[a] *Centre for Space Research, North-West University, Potchefstroom 2520, South Africa*
[b] *Centre for Astro-Particle Physics, University of Johannesburg, Auckland Park, 2092, South Africa*
[c] *Theoretical Division, Los Alamos National Laboratory, Los Alamos, NM 58545, USA*
[d] *Astrophysics Science Division, NASA Goddard Space Flight Center, Greenbelt, MD 20771, USA*
[e] *Universities Space Research Association (USRA), Columbia, MD 21046, USA*
[f] *University of Maryland, College Park (UMDCP/CRESST), College Park, MD 20742, USA*
[g] *College of Science, George Mason University, Fairfax, VA 22030, resident at Naval Research Laboratory, Washington, DC20375, USA*

E-mail: monicabarnard77@gmail.com

Recent detection of the Vela pulsar in the GeV band up to ~100 GeV by both H.E.S.S. and the *Fermi* Large Area Telescope provides evidence for a curved spectral component in this band, distinct from the TeV pulsed emission seen by H.E.S.S. up to ~7 TeV. We interpret these GeV pulsations to be the result of curvature radiation due to primary particles in the pulsar magnetosphere, primarily the current sheet. We present predictions of energy-dependent light curves and phase-resolved spectra using an extended slot gap and current sheet model in a force-free magnetosphere, invoking a step function for the accelerating electric field as motivated by kinetic simulations. Our refined calculation of the curvature radius of particle trajectories in the lab frame impacts the particle transport and resulting light curves and spectra. Our model reproduces the decrease of flux of the first peak versus the second one (P1/P2 effect), evolution of the bridge emission, near constant phase positions of peaks, and narrowing of pulses with increasing energy. We isolate the distribution of Lorentz factors and curvature radii of trajectories associated with the first and second γ-ray light curve peaks. The median values of these quantities are slightly larger for the second peak, leading to larger spectral cutoffs (i.e., a 'harder' second peak), and thus explaining the P1/P2 effect.

37[th] *International Cosmic Ray Conference (ICRC 2021)*
July 12th – 23rd, 2021
Online – Berlin, Germany

*Presenter

PoS(ICRC2021)685

1. Introduction

Discovery of γ-ray pulsations from four pulsars by ground-based Cherenkov telescopes has birthed a new era in pulsar science. MAGIC detected pulsations from the Crab pulsar up to 1 TeV [1], H.E.S.S.-II detected pulsations from Vela in the sub-20 GeV to 100 GeV range [2], H.E.S.S. observed pulsed TeV emission from Vela (H.E.S.S. Collaboration, in preparation), H.E.S.S.-II detected pulsations from PSR B1706−44 in the sub-100 GeV energy range [3], and MAGIC observed pulsed emission from the Geminga pulsar between 15 GeV and 75 GeV [4]. As the photon energy E_γ is increased above several GeV, the main light curve peaks of Crab, Vela and Geminga remain at the same phase positions, the intensity ratio of the first to second peak (P1/P2) decreases for Vela and Geminga, the inter-peak "bridge" emission evolves for Vela, and the peak widths decrease for Crab [5], Vela [6] and Geminga [7]. The P1/P2 vs. E_γ effect was also seen by *Fermi* for a number of pulsars [8, 9].

Recent theory developments include global magnetospheric models such as the force-free (FF; [10]) inside and dissipative outside (FIDO) model (e.g., [11–13], equatorial current sheet models (e.g., [14]), the striped-wind models (e.g., [15]), and kinetic / particle-in-cell simulations (PIC; [16–18]). Some studies using the FIDO models assume that particles are accelerated by induced E-fields in dissipative magnetospheres and produce GeV emission via curvature radiation (CR; e.g., [11, 12]). Conversely, in some of the wind or current-sheet models, high-energy (HE) emission originates beyond the light cylinder via synchrotron radiation (SR) by relativistic, hot particles that have been accelerated via magnetic reconnection inside the current sheet [e.g., 15]. Given this ongoing debate, we explain the GeV spectrum and light curves of Vela as measured by *Fermi* and H.E.S.S. by modelling the E_γ-dependent light curves (and P1/P2 signature) in the CR regime of synchro-curvature (SC) radiation. We hope to probe whether this effect can serve as a potential discriminator between emission mechanisms and models.

2. Model Description and Improvements

2.1 A 3D Pulsar Emission Model

Using the emission model of [19, 20], we study the full particle transport, but focus on the CR emission component by primary particles. This model assumes a 3D FF B-field as the basic magnetospheric structure, approximating the geometry of field lines implied by the dissipative models that require a high conductivity in order to match observed γ-ray light curves [12, 21]. Both primary particles (leptons) and electron-positron pairs are injected at the stellar surface. The primaries radiate CR and some of these γ-ray photons are converted into pairs in the intense B-fields close to the star. The primaries are injected with a low initial speed and are further accelerated along the B-field lines by a constant parallel E-field $E_\parallel$ (used as a free parameter in this model) in an extended slot gap (SG) reaching beyond the light cylinder into the current sheet. Using an independent code, we calculate a polar cap (PC) pair cascade that develops just above the neutron star surface, since the pairs radiate SR and the primaries CR, leading to further generations of particles with lower energies. The resulting pair spectrum is injected at the stellar surface.

2.2 Improved Particle Trajectory Calculations

We refine the previous first-order calculation of $\rho_{\rm c}$ along the electron (or positron) trajectory in the lab frame, assuming that all particles injected at the footpoint of a particular B-field line follow the same trajectory, independent of their energy, since they are quickly accelerated to relativistic energies by the unscreened E-field. We take into account both a longitudinal motion of the particles, as well as a perpendicular $\mathbf{E} \times \mathbf{B}$ drift in the lab frame.

To calculate the electron's trajectory as well as its associated curvature radius $\rho_{\rm c}$ in the lab frame, we used a small, fixed step size ds (where s is the arclength) along the B-field line. The first derivative along the trajectory indicates the direction of the particle's longitudinal motion. Next, we smooth the directions using s as the independent variable. Second, we match the unsmoothed and smoothed directions of the electron trajectory at particular s values to get rid of unwanted "tails" at low and high altitudes, introduced by the use of a Gaussian kernel density estimator (KDE, [22]) smoothing procedure. Third, we use a second-order method involving interpolation by a Lagrange polynomial to obtain the second-order derivatives of the positions along the trajectory as a function of s [23]. Lastly, we match $\rho_{\rm c}$ calculated using smoothed and unsmoothed directions to eliminate "tails" in $\rho_{\rm c}$ at low and high altitudes, as before. Having a pre-calculated $\rho_{\rm c}$ in hand, for a fine division in s along any particular B-field line, we then interpolate $\rho_{\rm c}$ in the particle transport calculations to accommodate an adaptive, variable-ds approach that is used to speed up the transport calculations, without losing accuracy of the trajectory. The improved calculation smooths out some instabilities in $\rho_{\rm c}(s)$.

3. Isolating the Spatial Origin of Emission for Each of the Light Curve Peaks

The relative fading of P1 vs. P2 with E_γ seems to be a common characteristic of HE light curves. We have been able to reproduce this with the code. To probe the origin of this effect, it is necessary to isolate the spatial origin of each light curve peak and study key parameters in these regions. We start by isolating each peak on the phase plot using increasingly smaller observer angle ζ and rotational phase ϕ bins, and then apply "reverse mapping" to uncover the emission's spatial position. For a given magnetic inclination angle $\alpha = 75^\circ$, we generated phase plots (see Figure 1 in [24]) for the Vela pulsar. We inject the primaries into a roughly annular SG situated between $r_{\rm ovc} = 0.90$ and $r_{\rm ovc} = 0.96$ (in units of PC radius; [20, 25]), and divide the cross section of the surface projection of the SG situated near the rim of the PC into 7 rings, with each ring having 360 azimuthal segments. We additionally set $ds = 10^{-3} R_{\rm LC}$ (the light cylinder radius where the corotation speed equals the speed of light c) with a corresponding KDE smoothing parameter $h = 50ds$.

We calculate the emission from the northern rotational hemisphere $\dot{N}'_\gamma(\phi, \zeta)$ only. The contribution of the emission from the southern hemisphere $\dot{S}'_\gamma$ is obtained by taking into account the symmetry with respect to the centre of the star (i.e., $\dot{S}'_\gamma = \dot{N}'_\gamma(\phi + 180^\circ, 180^\circ - \zeta)$)). The implication for calculations of, e.g., the histogram of the local values of $\rho_{\rm c}$ as done in Section 4, is that one has to carefully keep track of the (ϕ, ζ) coordinates of each peak, and map them back onto the northern-hemisphere caustic Thus one can perform the reverse mapping to find the spatial coordinates of the emission associated with each peak.

PoS(ICRC2021)685

4. Results

4.1 Phaseplots, Light Curves and Spectra for the Optimal and Non-optimal Parameters

We first perform a preliminary parameter study to search for an optimal combination of α, $\zeta_{\rm cut}$, and a constant acceleration "rate" (acceleration per unit length) $R_{\rm acc} = eE_{\parallel}/m_{\rm e}c^2$ cm^{-1} (with e the electron charge, $m_{\rm e}$ the electron mass, and $m_{\rm e}c^2$ the rest-mass energy), calibrated against *both* the observed HE light curves *and* spectra measured by *Fermi* and H.E.S.S. II; subsequently, we will consider the local environments where the respective light curve peaks originate (Section 4), given these optimal parameters. We consider two cases, based on either a constant or a two-step parametric accelerating $E_{\parallel}$-field, independent of the azimuthal angle $\phi_{\rm PC}$, ζ and radial distance r. Thus, we choose (and subsequently refer to this as scenario 1 and scenario 2): (1) a constant $R_{\rm acc}$ from the stellar surface and into the current sheet (see [19]), and (2) a two-valued $R_{\rm acc}$, where $R_{\rm acc,low}$ occurs inside, and $R_{\rm acc,high}$ outside the light cylinder (see [20]). The two-step function for the accelerating $E_{\parallel}$ is motivated by global dissipative models [11–13] and kinetic PIC models [18]. In what follows, we set $\alpha = 75^{\circ}$, and $\zeta_{\rm cut} = 65^{\circ}$, $R_{\rm acc} = 0.25$ cm^{-1} and a flux normalisation factor of $5J_{\rm GJ}$ for scenario 1, and $R_{\rm acc,low} = 0.04$ cm^{-1}, $R_{\rm acc,high} = 0.25$ cm^{-1}, and $10J_{\rm GJ}$ for scenario 2.

We indicate different energy ranges (with the minimum E_{γ} increasing from top to bottom), with the first panel showing light curves for a full HE range $E_{\gamma} \in (100~\text{MeV}, 50~\text{GeV})$. In both scenarios, four main trends are evident in our optimal fits to the light curves as they evolve with E_{γ}. First, the model peaks remain at the same phase. Second, the intensity ratio of P1 relative to P2 decreases as E_{γ} increases in some cases. Third, the bridge emission fades at higher energies, possibly reflecting its softer spectrum and its origin at lower altitudes. Lastly, the pulse width decreases with an increase in E_{γ}. It is encouraging that the model can broadly reproduce these observational trends. In Figure 1 we show the energy-dependent phase plots and accompanying light curves for our optimal fit, for both scenarios. For scenario 1 (left phase plot) the bridge and most of the off-peak emission disappears with increasing E_{γ}, although the light curve peak positions for both scenarios remain roughly stable. The other light curve trends mentioned above are also visible.

To test the robustness of the P1/P2 vs. E_{γ} effect, we studied the light curves at $\zeta_{\rm cut} = 40^{\circ}$ to obtain a counter-example (see Figure 8 in [24]). These light curves have a different emission structure than those in Figure 1, due to a different spatial origin of the emission. A similar study was done by [11] assuming a FIDO model to show that the P1/P2 effect is common, but not universal, since a change in geometry can reverse the effect.

In Figure 2, the phase-averaged and phase-resolved spectra are shown for the optimal parameters, i.e., $\alpha = 75^{\circ}$ and $\zeta_{\rm cut} = 65^{\circ}$. The model spectra fit the *Fermi* LAT points for both scenarios fairly well. In the first and second scenario, the phase-resolved spectra of P1 and P2 are roughly equal in flux. For P2, the spectral cutoff energy $E_{\gamma,\rm CR}$ remains larger, with the predicted cutoff being a few GeV. A larger cutoff for P2 compared to P1 is expected for this $\zeta_{\rm cut}$ value, since the second light curve peak survives longer than P1 as E_{γ} increases.

4.2 Local Environment of Emission Regions Connected to Each Light Curve Peak

In order to isolate and understand the P1/P2 vs. E_{γ} effect seen in the light curves of Vela, we investigated the values of $E_{\gamma,\rm CR}$, $\rho_{\rm c}$ and Lorentz factor γ in the spatial regions where each

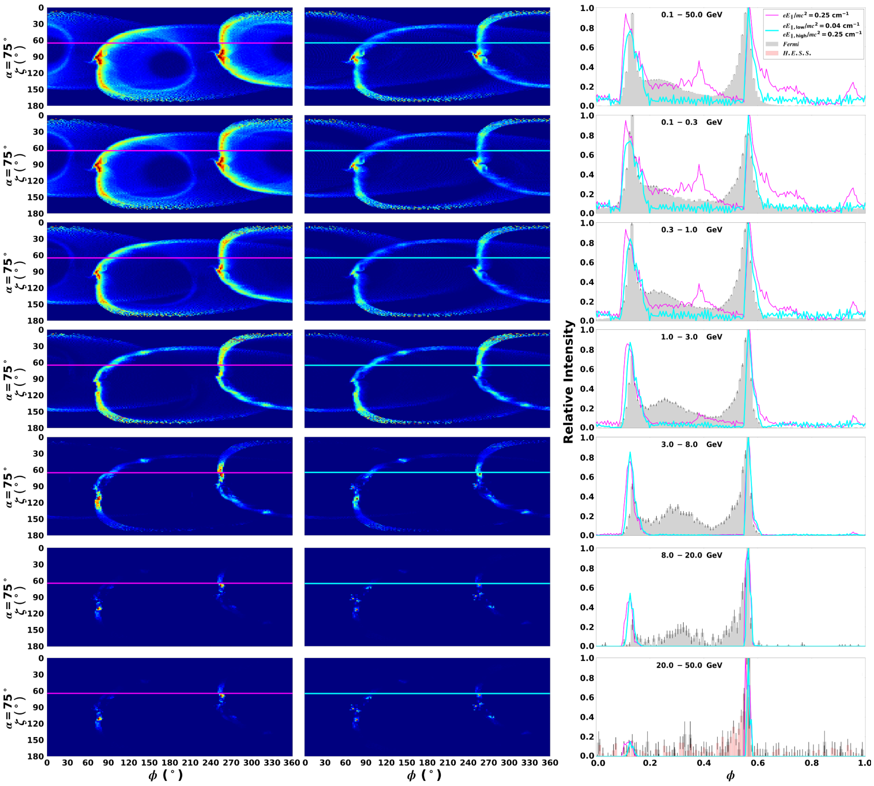

Figure 1: Energy-dependent phase plots and light curves for $\alpha = 75^\circ$ and $\zeta_{\rm cut} = 65^\circ$ and for the optimal $R_{\rm acc}$ for both the first (left column) and second (centre column) scenarios, plus their associated light curves (right column). The top panels are for the full E_γ-range, and each panel thereafter is for a different sub-band, as indicated by the labels in the light curve panels. Peaks were shifted by −0.14 to fit the *Fermi* LAT and H.E.S.S. data.

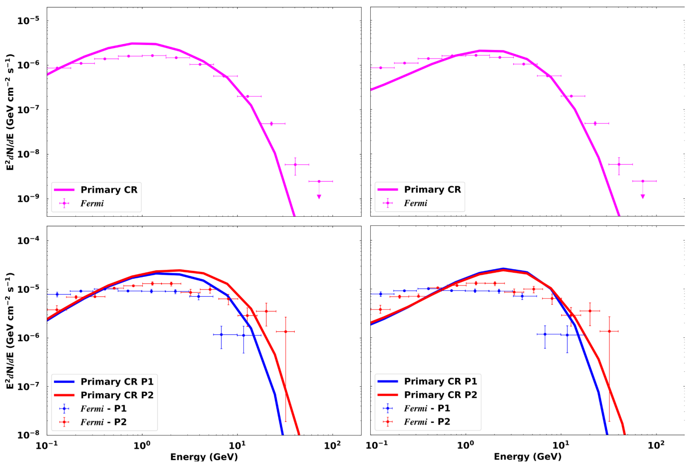

Figure 2: Phase-averaged (top panel) and phase-resolved (bottom panel) spectra for the refined $\rho_{\rm c}$ calculation, for $\alpha = 75^\circ$ and $\zeta_{\rm cut} = 65^\circ$. For the first scenario (left column), the flux is normalised using $5J_{\rm GJ}$ and for the second case (right column), it is normalised using $8.5J_{\rm GJ}$. The data points for the phase-average spectra are from [9] (see `http://fermi.gsfc.nasa.gov/ssc/data/access/lat/2nd_PSR_catalog/`), and the phase-resolved spectra are updated data are from [6].

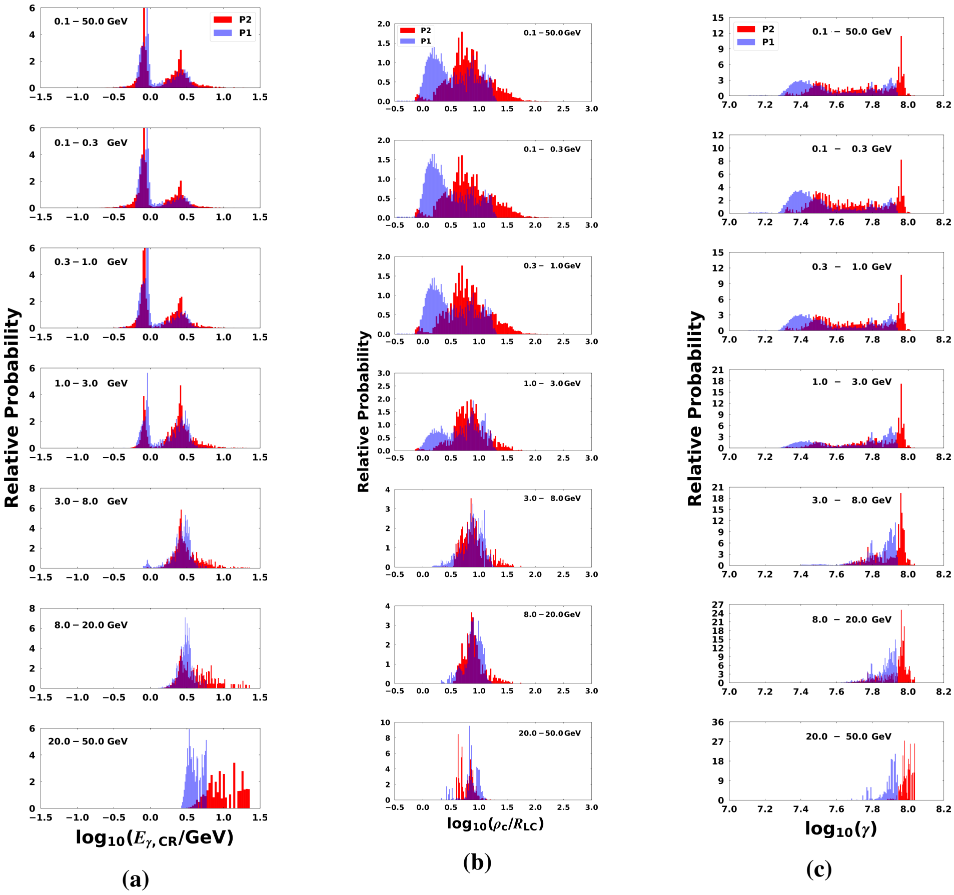

Figure 3: Example energy-dependent histograms for $\log_{10}(E_{\gamma,\rm CR}/\rm GeV)$, $\log_{10}(\rho_c/R_{\rm LC})$, and $\log_{10}(\gamma)$ for P1 (blue curve) and P2 (red curve), where all three cases represent scenario 1. The respective energy bands are indicated as labels in each panel.

model peak originates.We perform "reverse mapping" and accumulate the range of values that each of these quantities assume in the regions where the photons originate that make up P1 and P2, for a particular selected E_γ range. These binned quantities are presented as E_γ-dependent histograms below, where we scaled the frequency of occurrence of the quantities (signifying an unweighted probability) using the emitted photon emission rate $\dot{N}_\gamma$, to obtain a true (weighted) relative probability for each quantity.

In Figure 3(a) we show histograms for $\log_{10}(E_{\gamma,\rm CR}/\rm GeV)$, for different E_γ ranges. As an example we show scenario 1 (left column of Figure 3a; see [24] for scenario 2). There appears two bumps, for both peaks, at lower E_γ (up to $\sim$ 5 GeV), situated around $\log_{10}(E_{\gamma,\rm CR}/\rm GeV) \approx -0.2$ and 0.4. The lower bump disappears with increasing E_γ. The $\log_{10}(E_{\gamma,\rm CR}/\rm GeV)$ of P2 is relatively larger than that of P1 for scenario 1, as seen in the tail. This confirms what has already been seen in the light curves in Figure 1 and spectra in Figure 2: P2 survives with an increase in energy, since its spectral cutoff is relatively higher than that of P1. The $\log_{10}(E_{\gamma,\rm CR}/\rm GeV)$ of P2 reaches values as high as $\sim 10^{1.0} - 10^{1.4}$, with larger values reached in the first scenario, given the higher E-field.

In Figure 3b we show histograms of the relative probability as a function of $\log_{10}(\rho_c/R_{\rm LC})$ for

P1 (blue) and P2 (red). For the first scenario there appears a bump around $\log_{10}(\rho_c/R_{LC}) \approx 0$ to 0.5 for P1 at lower E_γ (up to ~ 3 GeV), which disappears with increasing E_γ. The accelerating E-field is relatively larger at lower altitudes, so that the particles can radiate in the GeV band from these lower altitudes characterised by lower values of $\log_{10}(\rho_c/R_{LC})$. Importantly, the $\log_{10}(\rho_c/R_{LC})$ of P2 is relatively larger than that of P1 as seen in the tail, with P2's associated ρ_c/R_{LC} reaching values as high as $\sim 10^{1.5} - 10^{3.0}$ cm (indicating relatively less curved orbits).

Similar to Figure 3a and Figure 3b, we show histograms of $\log_{10}(\gamma)$ in Figure 3c for different energy ranges and the first scenario. There appears a bump around $\log_{10}(\gamma) \approx 7.3 - 7.5$ for both peaks at lower E_γ (up to ~ 3 GeV), which disappears with increasing E_γ. There is also a peak in $\log_{10}(\gamma) \sim 8$ for P2 and the $\log_{10}(\gamma)$ of P2 is relatively larger than that of P1 as seen in the tail for this scenario.

5. Conclusions

There is an ongoing debate regarding the origin of the GeV emission detected from pulsars, it being attributed either to CR or SR (or even inverse Compton; see [26]). One way in which to possibly discriminate between these options is to model the energy-dependent light curves and phase-resolved spectra of several bright pulsars.

We presented a refined calculation of the ρ_c of particle trajectories, however, this refinement had a rather small impact, as the broad structure of caustics and light curves remained similar to what was found previously. We modelled E_γ-dependent light curves and spectra of the Vela pulsar in the HE regime assuming CR from primaries in an extended slot gap and current sheet model to see if we can explain the origin of the decreasing ratio of P1/P2 vs. E_γ, expecting that the answer may lie in a combination of the values of geometric and physical parameters associated with each peak. Since the light curves probe geometry, e.g., α, ζ and emission gap position and extent, while the spectrum probes both the energetics and geometry, we simultaneously fit both data sets with our model to obtain optimal fitting parameters.

We proceeded to isolate the P1/P2 effect by selecting photons that make up these two light curve peaks, and investigating the range of associated values of $E_{\gamma,\mathrm{CR}}$, ρ_c, γ and r/R_{LC}. We found that the phase-resolved spectra associated with each peak indicated a slightly larger spectral cutoff for P2, confirming that P2 survives with an increase in energy (also seen in energy-dependent histograms of $E_{\gamma,\mathrm{CR}}$). The reason for this became more clear upon discovery that both the ρ_c and γ were systematically larger for P2, for both scenarios. The $E_{\gamma,\mathrm{CR}}$ is proportional to ρ_c and γ, so the larger ρ_c and systematic dominance γ would explain the larger spectral cutoff for P2. In addition, we also found that the values of ρ_c and γ remained larger for P2 when only considering emission beyond the light cylinder; in particular, the largest values of these quantities occurred there, pointing to dominant emission from that region to make up the GeV light curves.

In summary, we found reasonable fits to the energy-dependent light curves and phase-resolved spectra of Vela, and our model that assumes CR as the mechanism responsible for the GeV emission. Similar future modelling of energy-dependent light curves and spectra within a striped-wind context that assumes SR to be the relevant GeV mechanism will be necessary to see if those models can also reproduce and explain these salient features in the case of Vela and other pulsars.

PoS(ICRC2021)685

References

[1] S. Ansoldi *et al.*, *Teraelectronvolt pulsed emission from the Crab Pulsar detected by MAGIC*, *A&A* **585** A133 (2016).

[2] H. Abdalla *et al.*, *First ground-based measurement of sub-20 GeV to 100 GeV γ-Rays from the Vela pulsar with H.E.S.S. II*, *A&A* **620** A66 (2018).

[3] M. Spir-Jacob *et al.*, *Detection of sub-100 GeV gamma-ray pulsations from PSR B1706-44 with H.E.S.S*, arXiv:1908.06464 (2019).

[4] V. A. Acciari *et al.*, *Detection of the Geminga pulsar with MAGIC hints at a power-law tail emission beyond 15 GeV*, *A&A* **643** L14 (2020).

[5] E. Aliu *et al.*, *Detection of Pulsed Gamma Rays Above 100 GeV from the Crab Pulsar*, *Science* **334** 69 (2011).

[6] A. A. Abdo *et al.*, *The Vela Pulsar: Results from the First Year of Fermi LAT Observations*, *ApJ* **713** 154 (2010).

[7] A. A. Abdo *et al.*, *Fermi-LAT Observations of the Geminga Pulsar*, *ApJ* **720** 272 (2010).

[8] A. A. Abdo *et al.*, *The First Fermi Large Area Telescope Catalog of Gamma-ray Pulsars*, *ApJS* **187** 460 (2010).

[9] A. A. Abdo *et al.*, *The Second Fermi Large Area Telescope Catalog of Gamma-Ray Pulsars*, *ApJS* **208** 17 (2013).

[10] C. Kalapotharakos & I. Contopoulos, *Three-dimensional numerical simulations of the pulsar magnetosphere: preliminary results*, *A&A* **496** 495 (2009).

[11] G. Brambilla, C. Kalapotharakos, A. K. Harding, & D. Kazanas, *Testing Dissipative Magnetosphere Model Light Curves and Spectra with Fermi Pulsars*, *ApJ* **804** 84 (2015).

[12] C. Kalapotharakos, A. K. Harding & D. Kazanas, *Gamma-Ray Emission in Dissipative Pulsar Magnetospheres: From Theory to Fermi Observations*, *ApJ* **793** 97 (2014).

[13] C. Kalapotharakos, A. K. Harding, D. Kazanas & G. Brambilla, *Fermi Gamma-Ray Pulsars: Understanding the High-energy Emission from Dissipative Magnetospheres*, *ApJ* **842** 80 (2017).

[14] J. Pétri, *High-energy emission from the pulsar striped wind: a synchrotron model for gamma-ray pulsars*, *MNRAS* **424** 2023 (2012).

[15] J. Pétri & G. Dubus, *Implication of the striped pulsar wind model for gamma-ray binaries*, *MNRAS* **417** 532 (2011).

[16] G. Brambilla, C. Kalapotharakos, A. N. Timokhin, A. K. Harding & D. Kazanas, *Electron-Positron Pair Flow and Current Composition in the Pulsar Magnetosphere*, *ApJ* **858** 81 (2018).

[17] B. Cerutti, A. Philippov & G. Dubus, *Dissipation of the striped pulsar wind and non-thermal particle acceleration: 3D PIC simulations*, arXiv:2008.11462 (2020).

[18] C. Kalapotharakos, G. Brambilla, A. Timokhin, A. K. Harding & D. Kazanas, *Three-dimensional Kinetic Pulsar Magnetosphere Models: Connecting to Gamma-Ray Observations*, *ApJ* **857** 44 (2018).

[19] A. K. Harding & C. Kalapotharakos, *Synchrotron Self-Compton Emission from the Crab and Other Pulsars*, *ApJ* **811** 63 (2015).

[20] A. K. Harding, C. Kalapotharakos, M. Barnard & C. Venter, *Multi-TeV Emission from the Vela Pulsar*, *ApJL* **869** L18 (2018).

[21] C. Kalapotharakos, D. Kazanas, A. K. Harding & I. Contopoulos, *Toward a Realistic Pulsar Magnetosphere*, *ApJ* **749** 2 (2012).

[22] E. Parzen, *On Estimation of a Probability Density Function and Mode*, The Institute of Mathematical Statistics (1962).

[23] J. D. Faires & R. L. Burden, *Numerical Methods*, 3$^{\text{th}}$ ed.; Brooks Cole (2002).

[24] M. Barnard, C. Venter, A. K. Harding & C. Kalapotharakos, *Probing the High-energy γ-ray Emission Mechanism in the Vela Pulsar via Phase-resolved Spectral and Energy-dependent Light Curve Modeling*, submitted to *ApJ* (2021).

[25] J. Dyks, A. K. Harding & B. Rudak, *Relativistic Effects and Polarization in Three High-Energy Pulsar Models*, *ApJ* **606** 1125 (2004).

[26] M. Lyutikov, N. Otte & A. McCann, *The Very High Energy Emission from Pulsars: A Case for Inverse Compton Scattering*, *ApJ* **754** 33 (2012).